D-MEW: Single-channel Validation of a Dual-material Capable Delta Melt Electrowriting Platform for High-speed Scaffold Fabrication

A. Deol[1], E. K. Moo[1], and I. Garces[1*]

[1] Department of Mechanical and Aerospace Engineering, Carleton University, Ottawa, Canada

* *Corresponding author (IrinaGarces@cunet.carleton.ca)*

Keywords: *Melt electrowriting (MEW); tissue-engineered scaffolds; delta kinematics; dual-material; polycaprolactone (PCL)*

1. Abstract

Melt electrowriting (MEW) is a high-resolution additive manufacturing (AM) capable of producing micron-scale fibres suitable for tissue engineering scaffolds. Accurate fibre deposition requires the collector translation speed relative to the printhead (RTS) to match the jet speed, a condition known as the critical translation speed (CTS). During high-speed printing, the accelerations required for directional changes can introduce a temporary mismatch between collector and jet velocities, reducing fibre placement accuracy. Delta kinematic platforms possess lower moving mass than conventional Cartesian platforms and may therefore reduce the effects of these acceleration-induced disturbances during directional changes. This study presents the D-MEW (Delta Melt Electrowriter), a delta kinematic platform integrating a dual-material syringe-based MEW printhead. As a prerequisite to dual-material operation, this study first evaluates single material MEW with polycaprolactone (PCL). The goal of this study is to characterize the effects of RTS, melt temperature, and turn geometry on deposition behaviour, and to establish baseline operating parameters for accurate fibre placement. Results demonstrated that fibre diameter decreased by 63–73% as RTS increased from 2.50 to 13.75 mm/s. CTS was identified between 6.25–8.75 mm/s for PCL processed at 88°C and between 8.75–11.25 mm/s for PCL processed at 90°C and 92°C. Turning performance was evaluated using the turning ratio, defined as the ratio of turning radius to inter-fibre spacing. A turning ratio of 2.0 provided the best spacing accuracy (312.75 ± 23.41 μm; target 300 μm) and deposition consistency. Fibre diameter was largely unaffected by turn geometry, indicating that fibre size and placement accuracy can be optimized independently. These results establish baseline operating parameters for the D-MEW platform and demonstrate the viability of delta kinematics for high-precision MEW.

2. Introduction

MEW is a high-resolution electrohydrodynamic AM process that combines aspects of melt electrospinning and extrusion-based additive manufacturing (EBAM). During printing, a high electric potential is applied to draw a molten polymer jet from the nozzle towards a grounded collector plate. By coordinating jet formation with collector motion, fibres can be deposited with high precision, enabling fibre diameters of 2-50 μm and placement accuracies of ±5–10 μm [1].

MEW's high resolution make it particularly well suited for tissue engineering (TE), where scaffolds require micron-scale fibres, interconnected porosity, and tunable mechanical properties to support cell growth and tissue regeneration [2]. The ability to tailor scaffold architecture is essential for mimicking native tissues, which are inherently heterogeneous with complex interface regions that exhibit variations in structural organization and composition [2]. Recent AM approaches aimed to replicate these features by incorporating gradients in both scaffold geometry and material composition; such approaches have resulted in enhanced mechanical stability and biocompatibility for bone TE applications [3]. Extending this concept to multimaterial MEW could enable spatial programming of scaffold properties by depositing different polymers within a single construct. For example, combining PCL and polylactic acid (PLA) could allow local stiffness to be tailored throughout a scaffold [4], while conductive or bioactive materials could be incorporated to create functional composite structures [5]. Similarly, sacrificial polymer fibres could be deposited within hydrogels to create microchannels for nutrient transport [6]. A multimaterial MEW system could potentially achieve these architectures in a single manufacturing step.

Despite its revolutionary nature, MEW remains limited by challenges associated with hardware complexity and material constraints. Custom MEW systems are inherently complex as they must combine high-voltage generation, thermal management, material delivery, and precise motion control within a single platform [7]. The high-voltage system must also be carefully isolated from heated and conductive components to ensure safe and stable operation [7]. Material compatibility presents an additional challenge, as only polymers with a sufficiently narrow viscosity window can form a stable Taylor cone: the cone-shaped meniscus at the nozzle tip that enables continuous jet formation under an electric field [8]. Prolonged heating also risks thermal degradation, further restricting the range of processable materials [8]. Many promising biocompatible and filler-modified polymers are unavailable as commercial filaments, making syringe-based MEW the preferred approach despite its increased hardware complexity [9]. Although several approaches to composite MEW have been reported, true multimaterial MEW remains largely unexplored. A dual-nozzle MEW system has been used to fabricate semi-woven structures using a single material [10]. Separately, a dual-mode platform combining filament-based MEW and EBAM enabled the fabrication of multiscale constructs from a single filament feedstock [11]. However, neither approach allowed in-situ switching between distinct polymer materials during printing, and such capability has not yet been demonstrated in MEW.

MEW performance is highly dependent on balancing strongly coupled processing parameters, including temperature, pressure, applied voltage, collector distance, and relative collector translation speed (RTS) [9]. Among these, RTS plays a critical role in controlling fibre diameter, with higher speeds generally producing finer fibres. However, achieving high RTS can be difficult as rapid changes in collector motion introduce inertial effects that disturb the polymer jet, reducing fibre deposition consistency [12]. These challenges have motivated the exploration of alternative kinematic configurations for MEW; previous studies have demonstrated fibre deposition onto complex three-dimensional collectors using a 5-axis MEW platform [13], and non-planar MEW using a 6-axis robotic arm [14]. Delta kinematic systems present another potential alternative; compared to conventional Cartesian platforms, delta systems use lower moving masses and distributed actuation. This enables higher accelerations and improved dimensional accuracy [15], making delta kinematics a compelling platform for high-speed MEW.

This work presents the D-MEW, a delta-kinematic MEW platform integrating a custom dual-material syringe-based printhead. To support future multimaterial MEW through in-situ material switching, the present study first characterizes single-material PCL MEW by evaluating the effects of RTS, melt temperature, and turn geometry on fibre morphology and deposition accuracy.

3. Background

3.1. MEW Parameter Tuning

MEW fibre formation is governed by five coupled parameters: extrusion pressure, melt temperature, applied voltage, collector distance and RTS [16]. These parameters, as highlighted in Figure 1a, jointly determine jet stability and final fibre diameter. Extrusion pressure and melt temperature primarily influence polymer melt viscosity and flow rate, while applied voltage controls electrohydrodynamic jet stretching [3]. Collector distance affects both the electric field strength and the time available for jet thinning and cooling prior to deposition [3]. In general, increasing RTS and applied voltage reduces fibre diameter, while increasing pressure and temperature tends to increase fibre diameter [3]. However, as the parameters are strongly coupled and interact nonlinearly, achieving a target fibre diameter requires careful empirical optimization for each material system [10].

If operating conditions fall outside the stable processing window, defects may occur, such as those seen in Figure 1b. For example, excessive extrusion pressure or insufficient voltage can produce fibre pulsing, where unstable jet formation at the nozzle tip causes diameter fluctuations [17]. At excessively high temperatures, material viscosity can drop below the threshold required to maintain a stable Taylor cone, resulting in jet breakup or droplet formation [18]. As a result, MEW is highly sensitive to parameter perturbations and requires operation within a well-characterized processing window before dynamic effects such as high-speed motion and directional changes can be investigated.

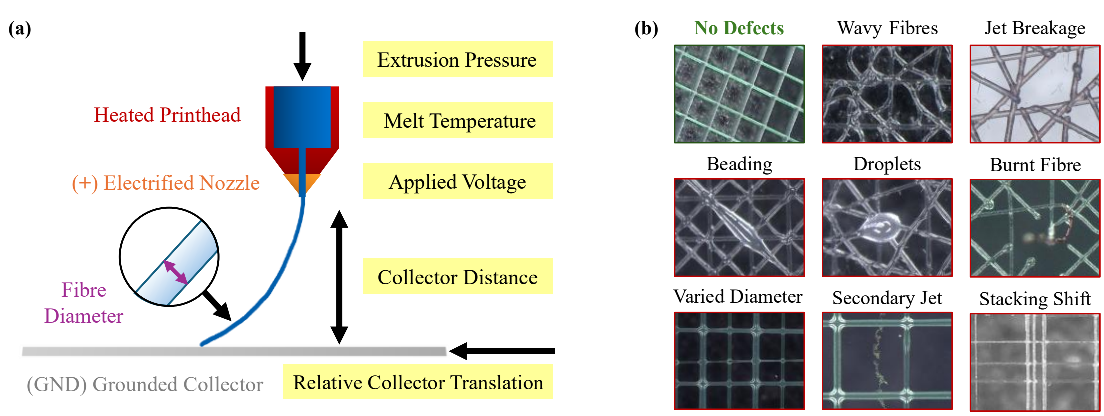

Figure 1. MEW operating conditions. (a) Schematic of 5 key tuning parameters for stable operation, (b) Characteristic defects.

3.2. Cartesian and Delta Kinematics

Common MEW systems use Cartesian motion architectures, where a gantry drives the printhead and collector along independent orthogonal axes. While more intuitive to control, these systems involve significant moving mass, particularly along axes that must frequently accelerate and decelerate during printing. At high speeds, the system's high inertia limits achievable acceleration and introduces mechanical disturbances during directional changes [19].

Delta motion architectures use three fixed actuators to drive a lightweight end-effector through parallel linkage arms. Actuators remain fixed at the platform base, substantially reducing the moving mass compared to relative Cartesian systems [15]. This theoretically reduces inertial effects during rapid motion and enables higher accelerations. Comparative studies of delta and Cartesian AM systems have reported improved surface finish quality for delta printers, though dimensional accuracy advantages remain geometry and calibration dependent [20].

3.3. Dynamic Motion Effects in MEW

Although material processing parameter optimization is essential, MEW performance also depends on maintaining stable instantaneous collector motion relative to the travelling polymer jet. Stable fibre deposition requires that the RTS (s_c) closely matches the jet travel speed (s_j) [1]. This condition is known as the critical translation speed (CTS) (s_c=s_j) (Figure 2b) [16]. When RTS falls below CTS (s_c<<s_j), excess material accumulates and the jet buckles, producing coiled or sinusoidal fibre patterns (Figure 2a) [21]. When RTS exceeds CTS (s_c>>s_j), the jet lags behind the collector, reducing deposition accuracy and increasing fibre placement error (Figure 2c) [16]. However, CTS is not fixed and shifts with operating conditions, requiring optimisation for each material system and platform configuration [16].

Maintaining CTS becomes increasingly difficult during directional changes. As the collector accelerates and decelerates, its instantaneous velocity temporarily deviates from the CTS condition, creating a mismatch between collector and jet speeds. These deviations cause local variation in fibre diameter and reduce placement accuracy [12]. The effect becomes more significant at elevated print speeds, where larger accelerations are required to execute a given toolpath [22] [16]. Reducing inertial effects in collector motion may help maintain more stable operation as RTS increases. Delta kinematic systems may better preserve stable collector-jet synchronization during dynamic motion, due to their lower moving mass.

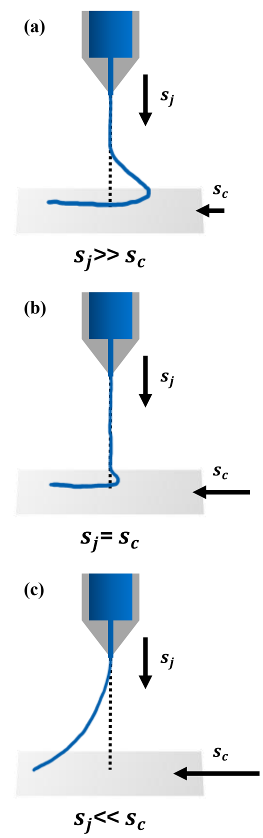

Figure 2. Effect of CTS on MEW jet deposition. (a) Buckling jet below CTS, (b) Stable jet at CTS, (c) Lagging jet above CTS.

4. Materials and Methods

4.1. D-MEW Printing Platform

The D-MEW system integrates a custom dual-material syringe-based MEW printhead into a Geeetech Delta Rostock Mini delta printer platform. The printhead was machined from aluminum and features a split-block design. The design supports independent flow of two molten polymer streams through a shared nozzle, with integrated heating to ensure uniform thermal conditions. For the single-channel validation presented, one flow path was sealed using a needle valve, such that only a single material channel was active during all experiments.

4.2. Materials

D3D Clear PCL filament (DigitMakers, Canada) was used for all experiments. The filament was cut into ~0.5 mm segments prior to processing.

4.3. Processing Parameters

Custom G-code toolpaths were generated using MATLAB for all print geometries. Samples were printed onto indium tin oxide (ITO) coated glass slides of 1.2 mm thickness. Slides were placed on the grounded collector plate. Material processing conditions are summarized in Table 1.

Table 1. PCL processing parameters for all experiments

Parameter	Unit	Value
Material		PCL
Nozzle Size	(mm)	0.1
Drying Temperature/Time	(°C/h)	45/8
Premelt Temperature/Time	(°C/h)	85/12
Collector Distance	(mm)	3.6
Collector Temperature	(°C)	42
Pressure	(bar)	1.0
Voltage	(kV)	5.00

Fibre Diameter Characterization: Samples consisted of a single layer of six parallel fibres with 600 µm spacing. RTS was varied from 2.50-13.75 mm/s in increments of 1.25 mm/s. Experiments were repeated at melt temperatures of 88°C, 90°C, and 92°C. Experiments were also repeated twice for each RTS-temperature condition, for a total of thirty tests to characterize the combined influence on fibre diameter.

Turning Ratio Characterization: To evaluate turning behaviour, a turning ratio (r/d) was defined as the ratio of turn-loop radius to inter-fibre spacing. Samples consisted of a single layer of ten parallel fibres with 300 µm spacing, at an arbitrarily fixed temperature of 90°C, pressure of 1.0 bar, and speed of 6.25 mm/s. Turning ratio was varied from 0.5-3.0 in increments of 0.5 (Section 5.2, Figure 4a). Experiments were repeated twice for each condition, for a total of twelve tests to evaluate the effect of turn geometry on inter-fibre spacing and fibre diameter consistency. Among subsequent fibres deposited, odd numbered fibres are categorized as Set A end even numbered fibres are categorized as Set B (Section 5.2, Figure 4c). Similarly odd and even numbered spacings are categorized as Sets A and B (Section 5.2, Figure 4c). Fibre sets and spacing sets are compared to analyze deposition consistency among alternating regions and toolpath directions.

4.4. Morphological Characterization

Samples were imaged using a Keyence VHX-X1 microscope at 50x and 100x magnification with coaxial illumination. Fibre diameter and inter-fibre spacing were quantified using custom MATLAB scripts developed for automated image analysis. Fibre diameters were determined from perpendicular distance measurements between detected fibre edges along the fibre length, while inter-fibre spacing was calculated from the distance between adjacent fibre centrelines. For the RTS–temperature study, ~11,700 fibre diameter measurements were collected per condition. For the turning ratio study, ~1,200 measurements were collected per condition for both fibre diameter and inter-fibre spacing analyses. Mean values, standard deviations (SD), and distribution statistics were calculated for each condition from the pooled datasets.

5. Results and Discussion

5.1. Collector Translation Speed Optimization

Figure 3a presents the effects of RTS on mean fibre diameter for melt temperatures of 88°C, 90°C, and 92°C. For all temperatures, fibre diameter decreased as RTS increased. At 88°C, fibre diameter decreased from 86.29±4.23 µm at 2.50 mm/s to 23.69±3.24 µm at 13.75 mm/s. Similarly, diameter decreased from 99.72±3.25 µm to 36.53±5.43 µm at 90°C, and from 97.67±4.67 µm to 30.01±5.29 µm at 92°C over the same RTS range.

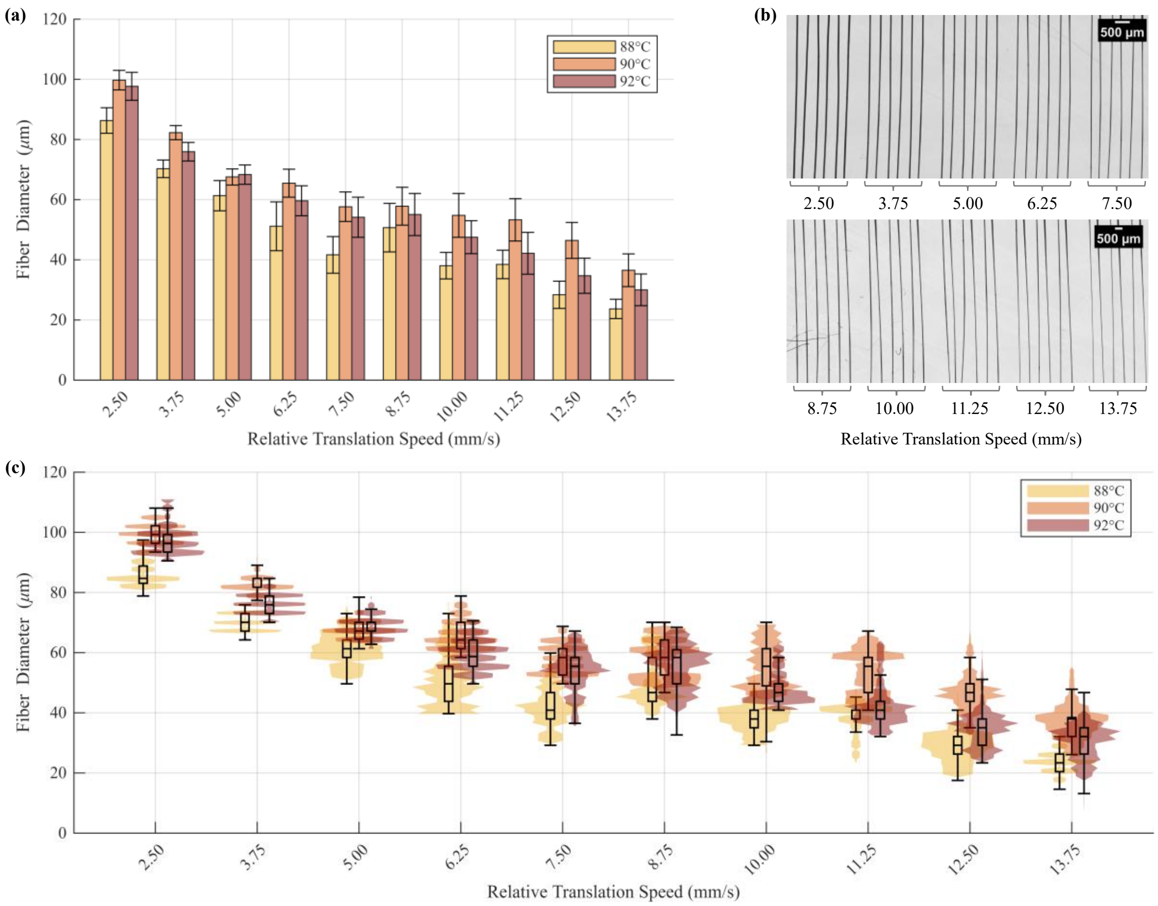

Figure 3. Effect of RTS on MEW PCL fiber diameter. (a) Mean fibre diameter (± 1 SD) for melt temperatures of 88°C, 90°C, and 92°C, (b) Representative fibre morphologies produced at 90°C across the investigated RTS range, (c) Distribution of fibre diameter measurements for melt temperatures of 88°C, 90°C, and 92°C.

As RTS increased by 11.25 mm/s, fibre diameter decreased by 73% for the 88°C, 63% for the 90°C, and 69% for the 92°C melts. Higher RTS draws the jet over a greater length per unit time, increasing stretching and reducing fibre diameter [16]. Additionally, fibres printed at 88°C were 13% smaller than those printed at 90°C at 2.50 mm/s, and 35% smaller at 13.75 mm/s, despite only a 2°C difference in melt temperature. This indicates that small differences in viscosity are amplified by jet stretching at elevated speeds. RTS is determined to be the primary parameter for controlling fibre diameter due to its greater impact and should be the first parameter adjusted when targeting a specific fibre size.

Figure 3a shows that fibres produced at 90°C exhibited the largest diameters, followed by 92°C, then 88°C. The observed diameter trends indicate that fibre formation is governed by multiple interacting mechanisms, such that increasing temperature does not result in a proportional increase in fibre diameter. Instead, an optimal processing window exists in which the combined effects of melt viscosity, material flow rate, electrohydrodynamic jet stability, and collector-induced stretching promote consistent fibre formation [16]. Higher melt viscosity at 88°C restricts material flow, reducing material deposition at the collector and resulting in the thinnest fibres across all RTS conditions. The slight diameter reduction observed at 92°C relative to 90°C suggests that the additional viscosity reduction at higher temperatures enhanced jet stretching, partially offsetting the increased flow rate. This behaviour is consistent with MEW processing near the lower viscosity limit of a material for stable Taylor cone formation, where increased melt fluidity increases jet sensitivity to electrohydrodynamic instabilities [8]. These results identify temperature as a secondary tuning parameter, fine-tuning the achievable fibre diameter range, whereas RTS remains the dominant factor governing fibre diameter. Since 88°C consistently produced the finest fibres, it is the preferred processing temperature when minimizing fibre diameter is the primary objective.

Figure 3c provides further insight into how the fibre diameter distributions evolve across the RTS range, revealing three distinct deposition regimes relative to CTS. These trends are further supported by the corresponding fibre morphologies shown in Figure 3b. At low RTS values (2.50–5.00 mm/s), diameter variation remained relatively low across all temperatures: SDs of 2.92–5.03 µm at 88°C, 2.32–3.25 µm at 90°C, and 3.07–4.67 µm at 92°C. Rather than the fully developed sinusoidal buckling reported in deep sub-CTS operation [17], excess material at these speeds appeared to accumulate directly within the fibre, producing thicker but relatively consistent deposits. This suggests operation near the lower boundary of the stable processing window, where the electric field and surface tension remain sufficient to maintain jet directionality, but the collector velocity is too slow to adequately stretch the jet.

As RTS increased towards CTS, diameter variation increased and reached a maximum SD of 8.11 µm at 88°C (RTS = 6.25 mm/s), 7.29 µm at 90°C (RTS = 10.00 mm/s), and 6.98 µm at 92°C (RTS = 8.75 mm/s). This regime corresponded to the straightest and most uniform fibre morphologies observed in Figure 3b. It is proposed that as jet and collector velocities become increasingly matched near CTS, excess material accumulation and jet lag are both minimized, producing the most geometrically accurate fibres. However, the jet becomes highly sensitive to small disturbances in jet velocity, melt flow, electric field strength, and platform motion under these conditions [16] [12]. This sensitivity may be further amplified by the fixed voltage used in this study, which may not be set high enough to fully stabilize the jet under near-CTS conditions where electrohydrodynamic forces play a greater role in maintaining stable deposition [16].

Above CTS, diameter variation declined as the collector increasingly outran the jet, producing a growing displacement between the jet deposition point and the programmed toolpath. This jet lag became particularly evident during directional changes, where the jet was unable to respond instantaneously to changes in collector motion. As a result, fibre placement accuracy deteriorated and morphological irregularities became more pronounced despite continued reductions in mean fibre diameter, as observed in Figure 3b. This above-CTS behaviour directly motivates the turn geometry investigation presented in Section 5.2.

Based on diameter variation trends and visual fibre morphology, CTS was estimated between 6.25–8.75 mm/s for 88°C and 8.75–11.25 mm/s for 90°C and 92°C. Simultaneous optimization of voltage with RTS to reduce near-CTS diameter variation is identified as a direction for future work. The sensitivity of the jet near CTS also highlights the importance of low-inertia kinematics for maintaining deposition stability at high printing speeds. A direct comparison with an equivalent Cartesian MEW system under matched conditions would be required to isolate the specific contribution of the motion system and is therefore identified as a priority for future work.

5.2. Turning Ratio Optimization

Figure 4 evaluates the effect of turn ratio (r/d) on deposition consistency. The critical turning ratio (CTR) was defined as the minimum turn geometry that allows disturbances caused by a directional change to stabilize before deposition of the subsequent fibre. Figure 4a illustrates the range of turn ratios investigated (r/d = 0.5-3.0), while Figure 4c defines the alternating spacing and fibre diameter measurements used for analysis (Sets A and B), corresponding to alternating sets of successive deposition paths through the turning region. Representative optical microscopy images of deposited fibres at turn ratios below, approximately at, and above the CTR are presented in Figure 4b.

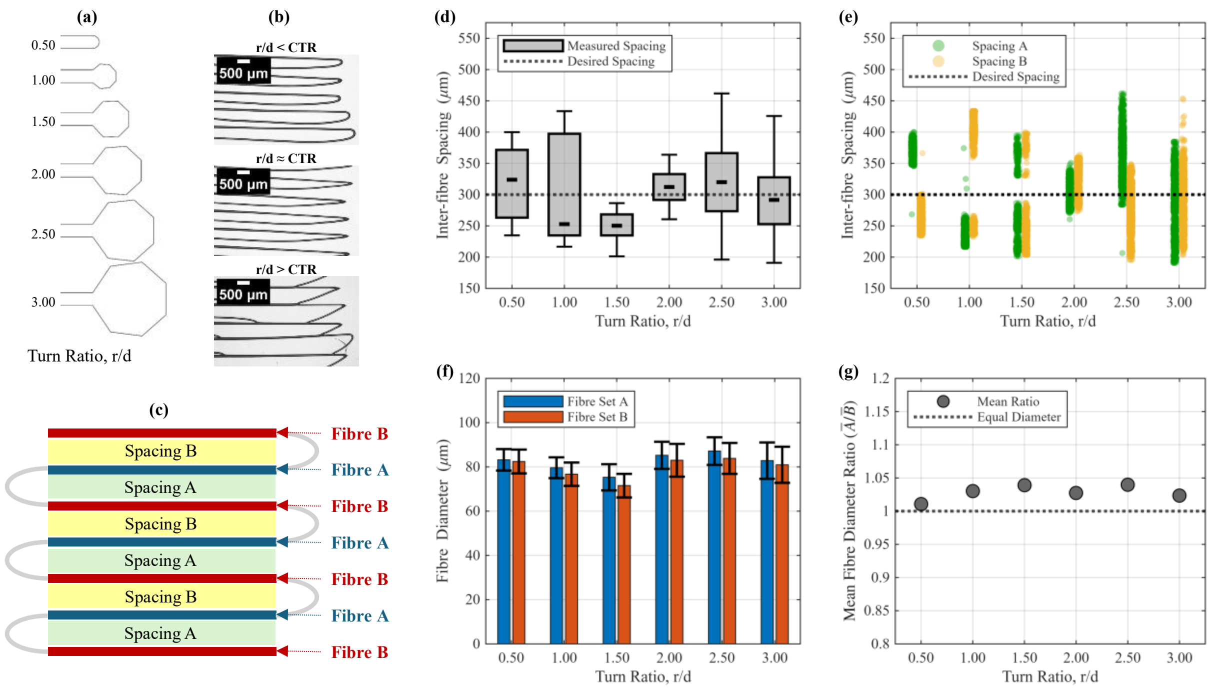

Figure 4. Effect of turn ratio (r/d) on MEW PCL fibre deposition accuracy. (a) Schematic representation of turn ratio G-code, (b) Representative optical microscopy images of deposited fibres at turn ratios below, approximately at, and above CTR, (c) Schematic of alternating Spacing A & B and Fibres A & B designations, (d) Distribution of overall inter-fibre spacing relative to desired spacing of 300 µm, (e) Distribution of alternating sets of inter-fibre spacing relative to desired spacing of 300 µm, (f) Mean fibre diameter (± 1 SD) of alternating fibre sets, (g) Ratio of mean fibre diameter sets (A/B).

Turn loop geometry strongly influenced the ability of the deposited fibres to maintain the programmed inter-fibre spacing of 300 µm. As shown in the overall distributions in Figure 4d, and the alternating spacing sets in Figure 4e, both spacing accuracy and variability were highly dependent on r/d. Mean spacing varied from 242.92±19.93 µm at r/d = 1.5 to 318.69±58.95 µm at r/d = 2.5. Although r/d = 1.0 produced a mean spacing of 300.83±79.91 µm, the closest to the target value, it also exhibited the highest variability and a clearly bimodal distribution. This indicates that the jet was not recovering consistently between successive directional changes. In contrast, r/d = 1.5 and 2.0 produced the most consistent spacing distributions, with SDs of only 19.93 µm and 23.41 µm respectively, reflecting more repeatable fibre placement through the turning region.

These behaviours define three distinct deposition regimes, as exemplified in Figure 4b. At low turn ratios (r/d = 0.5-1.0), the turn is too small to allow the jet to fully reorient and restabilize before the next fibre is deposited. The residual jet displacement from the sharp directional change persists into the next deposition path, producing alternating regions of fibre convergence and divergence, as reflected in the bimodal spacing distributions of Figure 4e. At intermediate ratios (r/d = 1.5-2.0), the longer turn loop provides sufficient time for the jet to recover, enabling more consistent path following and improved deposition uniformity. However, at r/d = 1.5, a systematic offset below the target spacing occurs, suggesting over-constrained geometric correction within the loop. At larger turn ratios (r/d = 2.5–3.0), spacing variability increased again as the excessive loop length delays recovery of the fibre trajectory following the directional change, reducing placement consistency.

Fibre diameter was comparatively insensitive to turn ratio, as seen in Figures 4f–g. Mean diameter of the alternating Fibre Sets A and B ranged from 75–87 µm and 72–84 µm respectively across all conditions. Fibre Set A remained marginally larger than Fibre Set B across all conditions, with diameter ratios ranging from 1.009 to 1.053. Given the small magnitude of this asymmetry, it is likely attributable to natural process variability rather than a systematic effect of turn geometry. This insensitivity to turn geometry confirms that fibre diameter and placement accuracy are governed by somewhat independent parameters. Among the tested parameters, diameter is primarily set by RTS and temperature, while spatial consistency is controlled by turn geometry. This decoupling simplifies parameter optimization for scaffold designs, which require both precise fibre dimensions and accurate spatial registration.

Overall, r/d = 2.0 provided the best performance, combining inter-fibre spacing accuracy, low variability, and stable fibre diameter. This condition produced a mean spacing of 312.75 ± 23.41 µm with a narrow, unimodal distribution and is therefore identified as the CTR for the current processing conditions. While reduced platform inertia may improve motion performance, directional changes still disturb jet deposition through transient velocity mismatches between the collector and the polymer jet. These disturbances are not eliminated by platform kinematics alone, and appropriate turn geometry remain necessary to maintain deposition consistency.

6. Conclusion

This study presented the D-MEW platform, a delta kinematic MEW system developed to support future dual-material scaffold fabrication, and established baseline operating parameters through single-channel PCL printing. RTS was identified as the primary parameter controlling fibre diameter, with reductions of 63–73% observed across an 11.25 mm/s increase in speed.

Temperature acted as a secondary tuning parameter, with 88°C producing the finest fibres across all RTS conditions due to higher melt viscosity promoting greater jet thinning. CTS was identified between 6.25–8.75 mm/s for 88°C and 8.75–11.25 mm/s for 90°C and 92°C, representing the optimal operating window for consistent fibre deposition. Turn loop geometry was found to independently govern spatial deposition accuracy without meaningfully affecting fibre diameter. This decoupling is practically significant, as it allows fibre size and placement accuracy to be optimized separately when designing scaffold toolpaths. A CTR of r/d = 2.0 provided the most accurate spacing and consistent deposition, producing a mean inter-fibre spacing of 312.75±23.41 µm against a target of 300 µm. Together, these results demonstrate that stable, geometrically consistent MEW is achievable using a delta kinematic architecture. Successful operation across the CTS regime and through repeated directional changes supports the feasibility of the D-MEW platform for future multimaterial scaffold fabrication. A direct comparison with a Cartesian MEW system under matched parameters is identified as the next step to quantify the specific motion performance benefits of delta kinematics in MEW.

7. References

[1] T. D. Brown, P. D. Dalton, and D. W. Hutmacher, "Direct writing by way of melt electrospinning," *Adv. Mater.*, vol. 23, no. 47, pp. 5651–5657, 2011.
[2] C. Snow et al., "A detailed guide to melt electro-writing for tissue engineering applications," *Biofabrication*, 2025.
[3] S. M. Bittner et al., "Fabrication and mechanical characterization of 3D printed vertical uniform and gradient scaffolds for bone and osteochondral tissue engineering," *Acta Biomater.*, vol. 90, pp. 37–48, 2019.
[4] M. Shahverdi et al., "Melt electrowriting of PLA, PCL, and composite PLA/PCL scaffolds for tissue engineering application," *Sci. Rep.*, vol. 12, p. 19935, 2022.
[5] J. H. Y. Chung, S. Sayyar, and G. G. Wallace, "Effect of graphene addition on polycaprolactone scaffolds fabricated using melt-electrowriting," *Polymers*, vol. 14, no. 2, p. 319, 2022.
[6] M. Ryma et al., "A print-and-fuse strategy for sacrificial filaments enables biomimetically structured perfusable microvascular networks with functional endothelium inside 3D hydrogels," *Adv. Mater.*, vol. 34, no. 26, p. 2200653, 2022
[7] A. Reizabal et al., "How to design, develop and build a fully-integrated melt electrowriting 3D printer," *Addit. Manuf.*, vol. 60, p. 102998, 2022.
[8] J. C. Kade and P. D. Dalton, "Polymers for melt electrowriting," *Adv. Healthcare Mater.*, vol. 10, no. 1, p. 2001232, 2021.
[9] P. G. Saiz et al., "Materials and strategies to enhance melt electrowriting potential," *Adv. Mater.*, vol. 36, no. 14, p. 2312084, 2024.
[10] R. S. Diaz, E. M. De-Juan-Pardo, and P. D. Dalton, "Semi-woven structures via dual nozzle melt electrowriting," *Macromol. Mater. Eng.*, vol. 308, no. 3, p. 2200526, 2023.
[11] S. Luposchainsky et al., "Filament-based melt electrowriting enables dual-mode additive manufacturing for multiscale constructs," *Small Sci.*, vol. 4, no. 2, p. 2300021, 2024.
[12] P. Mieszczanek, T. M. Robinson, P. D. Dalton, and D. W. Hutmacher, "Convergence of machine vision and melt electrowriting," *Adv. Mater.*, vol. 33, no. 35, p. 2100519, 2021.
[13] L. Terranova et al., "A versatile 5-axis melt electrowriting platform for unprecedented design freedom of 3D fibrous scaffolds," *Addit. Manuf.*, vol. 89, p. 104431, 2024.
[14] S. Luposchainsky, P. G. Saiz, A. Reizabal, S. Lanceros-Mendez, and P. D. Dalton, "Melt electrowriting of poly(dioxanone) filament using a multi-axis robot," *Macromol. Mater. Eng.*, vol. 307, no. 10, p. 2200450, 2022.
[15] M. Beigmoradi, M. Bodaghi, and A. Yazdanpanah, "Analysis of multiple print-head displacement mechanisms in 3D space for material extrusion machine," *3D Print. Addit. Manufacturing*, 2024.
[16] T. M. Robinson, D. W. Hutmacher, and P. D. Dalton, "The next frontier in melt electrospinning: Taming the jet," *Adv. Funct. Mater.*, vol. 29, no. 44, p. 1904664, 2019.
[17] G. Hochleitner, A. Youssef, A. Hrynevich, J. N. Haigh, T. Jungst, J. Groll, and P. D. Dalton, "Fibre pulsing during melt electrospinning writing," BioNanoMaterials, vol. 17, no. 3–4, pp. 159–171, 2016.
[18] X. Sun et al., "Challenges of high-temperature melt electrowriting: A study of EVOH printing," *Polymer*, vol. 318, p. 128518, 2025.
[19] E. E. Kopets, G. Y. Kolev, V. Vatnik, A. I. Karimov, and V. G. Rybin, "Mechanical vibration analysis of a gantry 3D printer," in *Proc. 2021 IEEE Conf. Russian Young Researchers Elect. Electron. Eng. (ElConRus)*, St. Petersburg, Russia, 2021, pp. 956–960.
[20] B. M. Schmitt, C. F. Zirbes, C. Bonin, D. Lohmann, D. C. Lencina, and A. C. S. Netto, "A comparative study of Cartesian and delta 3D printers on producing PLA parts," *Mater. Res.*, vol. 20, no. 2, pp. 883–886, 2018.
[21] G. Hochleitner, F. Chen, C. Blum, P. D. Dalton, B. Amsden, and J. Groll, "Melt electrowriting below the critical translation speed to fabricate crimped elastomer scaffolds with non-linear extension behaviour mimicking that of ligaments and tendons," *Acta Biomater.*, vol. 72, pp. 110–120, 2018.
[22] A. Hrynevich, I. Liashenko, and P. D. Dalton, "Accurate prediction of melt electrowritten laydown patterns from simple geometrical considerations," *Adv. Mater. Technol.*, vol. 5, no. 12, p. 2000772, 2020.